J Porous Mater (2017) 24:1383–1394
DOI 10.1007/s10934-017-0380-7

Differences in characteristics of Zr/SBA-15 and bimetallic Zr-La/SBA-15 prepared by sol–gel and hydrothermal methods

Chaowat Autthanit[1] · **Bunjerd Jongsomjit**[1]

Published online: 4 February 2017

Abstract In the present work, we report results of a comparative study of zirconium (Zr) and bimetal (Zr and La) containing in SBA-15 silica, which was prepared by conventional sol–gel and one-step hydrothermal methods. The structural and surface properties of all samples were characterized by low and high-angle XRD, nitrogen physisorption, FTIR, Raman, UV–Vis, SEM/EDX, TEM, and NH_3-TPD techniques. The experimental results demonstrated that the samples obtained from the sol–gel method retain the two-dimensional hexagonal order structure of SBA-15. Compared to samples obtained from the hydrothermal method, the pore system lacking long-range order was observed. The incorporation of Zr and bimetal (Zr and La) had an effect on the textural properties of both synthesized SBA-15 samples. This modified SBA-15 mesoporous samples still exhibited high specific surface area, large pore volume and narrow pore size distribution. Surface acidity in the SBA-15 silica suggests new active sites, especially Brønsted acid type, indicating its future potential applications when acid sites are required.

Keywords SBA-15 · Zirconium · Bimetal incorporation · Sol–gel · Hydrothermal · Characterization

✉ Bunjerd Jongsomjit
bunjerd.j@chula.ac.th

[1] Center of Excellence on Catalysis and Catalytic Reaction Engineering, Department of Chemical Engineering, Faculty of Engineering, Chulalongkorn University, Bangkok 10330, Thailand

1 Introduction

Ordered mesoporous silicas have attracted widespread interest in many frontier areas of science and technology due to their potential applications in various fields, such as adsorption, sensors, photonics, drug delivery, catalysis, and etc. [1]. During the last two decades, various mesoporous structures have been synthesized, which can be roughly classified into three categories based on the pore types; nearly spherical cage, cylindrical channel and bi-continuous channel [2]. This is better than the microporous zeolites, which present severe mass transfer limitations when large reactant molecules are involved, especially in liquid-phase systems for the synthesis of fine chemicals [3, 4]. Many reviews have summarized the catalytic applications of mesoporous silica [5–7] or mesoporous zeolite [8] as catalyst supports. There are many strategies for the design and synthesis of mesoporous catalysts, especially the characteristic features such as exceptionally high surface area, uniform and well-defined pores of nanoscale dimensions, which can be adjusted over a large range (2–20 nm) [9]. The high internal surface area of typically 400–900 m^2/g makes SBA-15 a well suited material for various applications. Not only because of its larger pores, but also thermal, mechanical and chemical resistance properties that make it a preferable choice to other types of catalyst [10]. However, pure mesoporous molecular sieves have no intrinsic catalytic activity due to the absence of heteroatom activity sites. It is necessary to replace part of the silicon in the structure onto the internal surface of the pores heteroatoms such as Ti, V, Al, Mo, Cr, Fe, into the framework by impregnation of active components or immobilization of active species with pre-determined structure. This is able to make the catalytically active solids with specific properties [11, 12]. Indeed, transition-metal incorporated mesoporous

silicas are of great interest because these metal functionalized materials may find use in catalysis, such as acid catalysis and base catalysis [13].

In particular, zirconium incorporated mesoporous silicas are particularly interesting because of the important applications of Zr-based materials in a wide variety of areas in heterogeneous catalysis. It is important to introduce an effective method to synthesize metal (M–O–Si) containing SBA-15. Salas et al. [14] investigated the surface acidity of the Zr-based mesoporous molecular sieves and found that SiO_2/ZrO_2 mesocomposites with worm-like pores could be obtained via a surfactant-templated or sol–gel method. The sample with low SiO_2/ZrO_2 molar ratio presents more Brønsted acid sites. Because the pure mesoporous molecular sieves lacks Brønsted acid sites, therefore, the incorporation of zirconium ions into the framework of the mesoporous molecular sieves is responsible for the formation of these Brønsted acid sites. In addition, many efforts have been made to improve the active sites by incorporation some dopants such as titania, niobia, lanthanum, tungsten oxide and molybdenum oxide. Sheng et al. [15] pointed out that La was incorporated in SBA-15 material by direct synthesis and post synthesis using two different lanthanum sources. The lanthanum nitrate is a suitable lanthanum source, which can match the hydrolysis rate of silicon precursor and composite materials possess larger specific surface area and uniform mesopore size distribution. The presence of anions in the synthesis mixture of mesoporous material is found to have a remarkable influence on their final structure, and hence, can be an important factor in the design of these materials. However, little attention has been paid to the synthesis and application of the SBA-15 materials containing bimetallic heteroatoms, which can introduce new catalytic sites into mesoporous materials. It is well known that bimetal (Zr and La) is incorporated in SBA-15 mesoporous materials with a desirable ordered two-dimensional hexagonal structure. This can create new active sites, which were synthesized by a direct hydrothermal method under a self-generated acidic condition in the absence of hydrochloric acid [16]. The improved catalyst activity has been suggested to be due to surface modification and changes of the interaction between metal and support.

Various synthetic pathways have been employed for the preparation of SBA-15 materials with different particle sizes and morphologies, such as hydrothermal method, sol–gel technique, solid state route [17], and microwave-hydrothermal process [18]. The sol–gel method has been proposed as the traditional method, but the precipitated powders obtained are amorphous in nature and further heat treatment is required for crystallization. Hydrothermal method is an alternative route for one-step synthesis of mesoporous silicas nanoparticles [19]. Particle morphology, crystalline phase, and surface chemistry of the products can be controlled by regulating precursor composition, reaction temperature, pressure, solvent property, and aging time [20, 21].

In the present work, we synthesized zirconium and bimetal (Zr and La) containing mesoporous silicas (SBA-15) via conventional sol–gel method to create a mesostructured form. However, the overall process of this method requires a long time period over 40 h [22, 23] and high temperature treatment, which may generate gaseous pollutants (such as CO_2 and NO_x) [13] with perhaps partially destroyed the ordered structure of the mesoporous material. For this reason, we used an alternative method called the one-step hydrothermal method without addition of hydrochloric acid for environmentally friendly to make new active sites. The relevant characterization techniques such as low and high-angle XRD, N_2 physisorption, FTIR, Raman, UV–Vis, SEM/EDX, TEM, and NH_3-TPD were carried out to reveal the physical and chemical properties of materials.

2 Materials and methods

2.1 Materials

The chemicals used for preparation of the catalysts were tetraethyl orthosilicate (TEOS) (98%, Aldrich), zirconium (IV) n-propoxide solution (70 wt% in 1-propanol, Aldrich), zirconyl chloride octahydrate (98%, Aldrich), lanthanum(III) nitrate hexahydrate (99.9%, Aldrich), Pluronic P-123 (average Mn ~5800 Da, Sigma-Aldrich) as structure directing agent, hydrochloric acid (HCl, 37%, Carlo Erba). Gases employed were He (99.99%, Air Liquide), H_2 (99.999%, Air Liquide), N_2 (99.9999%, Air Liquide), synthetic air (99.99%, Air Liquide), and NH_3 (99.9%, Air Liquide).

2.2 Preparation

2.2.1 Synthesis of SBA-15 was conducted by sol–gel method

First, the mesoporous SBA-15 silica was synthesized following the reported procedure by Cecilia et al. [24]. For the incorporation of zirconium containing mesoporous silicas (SBA-15), the structure-directing agent P-123 was dissolved in a 1.7 M hydrochloric acid aqueous solution, under magnetic stirring at 40 °C. Subsequently, TEOS (silica source) and zirconium n-propoxide were added dropwise, with a Si/Zr molar ratio of 5. The final molar composition of the synthesis gel was P-123/SiO_2/ZrO_2/HCl/H_2O = 1/55/11/350/11,100. For bimetallic containing SBA-15, lanthanum(III) nitrate hexahydrate was

added into above solution under similar procedure. The molar ratio of P-123/SiO_2/ZrO_2/$La(NO_3)_3{\cdot}6H_2O$/HCl/H_2O = 1/55/11/11/350/11,100. The resulting suspension was stirred at 40 °C for 72 h. The obtained sample was recovered by filtration, rinsed with deionized water until the pH of filtrate was constant, dried at 60 °C, and finally calcined in air at 550 °C for 6 h with a heating rate of 1 °C min^{-1}. The SBA-15 silica was denoted as SBA-15-*SG*, where *SG* indicates the sol–gel-derived method.

2.2.2 *Synthesis of SBA-15 was conducted by hydrothermal method*

All catalysts obtained by the hydrothermal method were performed according to the procedure of Liu et al. [16]. For the incorporation of zirconium containing SBA-15, 2 g of the structure-directing agent P-123, was dissolved in 100 g of deionized water under vigorous stirring at 35 °C for 2 h. Then, TEOS and zirconyl chloride octahydrate were added into above solution. The molar ratio of P-123/TEOS/H_2O/$ZrOCl_2{\cdot}8H_2O$ = 0.01/1/170/1. For bimetallic containing SBA-15, lanthanum(III) nitrate hexahydrate was added into above solution under similar procedure. The molar ratio of P-123/TEOS/H_2O/$ZrOCl_2{\cdot}8H_2O$/$La(NO_3)_3{\cdot}6H_2O$ = 0.01/1/170/1/1. The mixed solution was continuously stirred for 20 h. Finally, the gel was transferred into a Teflon-lined autoclave and heated at 100 °C for 24 h. The white product was filtered. The remaining catalyst was rinsed with deionized water and absolute ethanol until the pH become neutral and dried at 60 °C for 24 h. The structure-directing agent was removed from the as-synthesized product through a solvent extraction procedure using HCl/EtOH solution (1 g of sample in 5 mL/150 mL) for 24 h. The catalyst was obtained after drying at 105 °C for 24 h. The SBA-15 silica was denoted as SBA-15-*HT*, where *HT* indicates the hydrothermal-derived methods.

2.3 Characterization

Low-angle X-ray powder diffraction (XRD) patterns were collected on Bruker AXS Model D8 Discover X-ray diffractometer, using nickel-filtered Cu K_α as monochromatic X-ray radiation and a VÅNTEC-1 detector. Diffraction data were recorded at an interval of 0.01671 in the 2θ range of 0.5°–10°. The interplanar distance (d_{100}) was obtained by the Bragg's law using the position of the first X-ray diffraction line. High-angle XRD patterns of the catalysts were measured over an angle 2θ range of 10°–80° having the resolution of 0.02° and a step time of 0.2 s.

The surface area and average pore volume were determined by N_2-physisorption using Micromeritics ChemiSorb 2750 Pulse instrument. Measurement was performed at −196 °C and calculated according to the Brunauer-Emmet-Teller (BET) isotherm equation and a nitrogen molecule cross section of 16.2 Å. The pore size distributions were derived from the desorption profiles of the isotherms using the Barrett-Joyner-Halenda (BJH) method, based on the Kelvin Equation [25].

The IR spectra were recorded using Nicolet 6700 FTIR spectrometer in the range of 400–4000 cm^{-1} to identify specific structural characteristics of the chemical group from the vibration properties.

Raman spectroscopy was performed on a using a PE IR SPECTRUM ASCII PEDS 1.60 spectrometer with a 244 nm laser with experimental power of 3 W at a step length of 4 cm^{-1} in the range between 200 and 1400 cm^{-1}.

The UV–Vis spectra of the samples were collected on a Perkin Elmer Lamda-650. The powder sample was loaded into a quartz cell, and the spectra were collected over the wavelength of 200–600 nm with a step size at 1 nm reference to $BaSO_4$.

The morphology and elemental distribution over the catalyst surface were determined by scanning electron microscope (SEM) and energy dispersive X-ray spectroscopy (EDX). SEM and EDX were used to investigate the morphology and elemental distribution of catalysts, respectively using Hitashi mode S-3400N. Micrographs were taken at the accelerating voltage of 30 kV and magnification ranging from 1000 to 10,000 and the resolution of 3 nm. The SEM was operated using the secondary scattering electron (SE) mode. EDX was performed using Apollo X Silicon Drift Detector Series by EDAX.

The dispersion of all catalysts was observed using JEOL-JEM 200CX transmission electron microscope (TEM) operated at 200 kV. The samples were grounded, suspended in ethanol at room temperature, and dispersed with ultrasonic agitation. Then, an aliquot of the solution was dropped on a 3 mm diameter lacey carbon copper grid.

The temperature-programmed desorption of ammonia (NH_3-TPD) was carried out to evaluate the total surface acidity of the catalysts. The catalyst (80 mg) was evacuated with helium at 550 °C, and then ammonia was adsorbed at 100 °C. Finally, the NH_3-TPD was performed by raising the temperature from 100 to 550 °C, under a helium flow of 40 mL min^{-1}, with a heating rate of 10 °C min^{-1}. The amount of ammonia in effluent was measured via the thermal conductivity detector (TCD) as a function of temperature [24].

3 Results and discussion

X-ray diffraction was used to identify crystalline phases present in these samples. The XRD patterns at low-angle of all samples obtained by the sol–gel method are shown in Fig. 1a. The successful formation of well-ordered

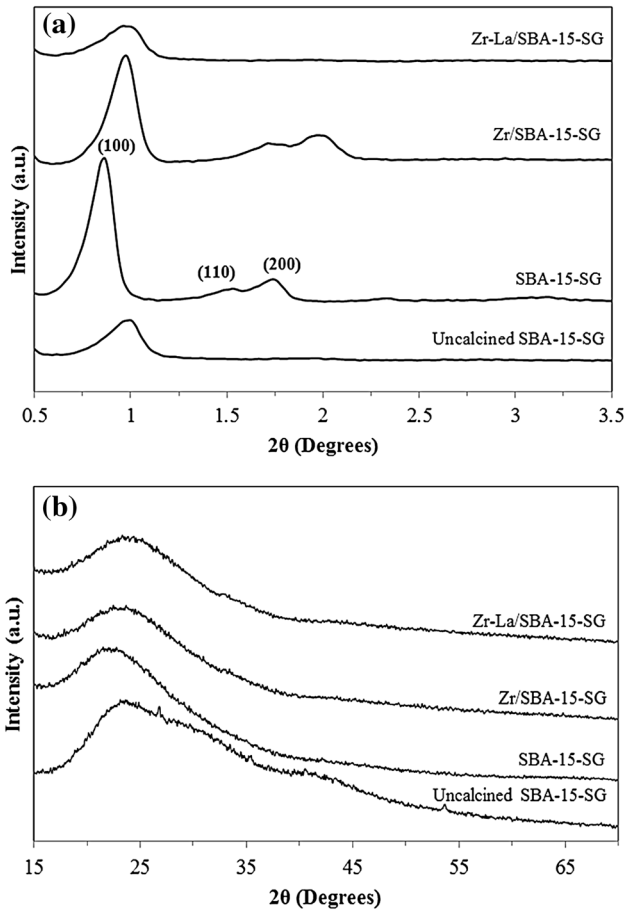

Fig. 1 XRD patterns of all samples obtained from the sol–gel method at low-angle (**a**) and high-angle (**b**) regions

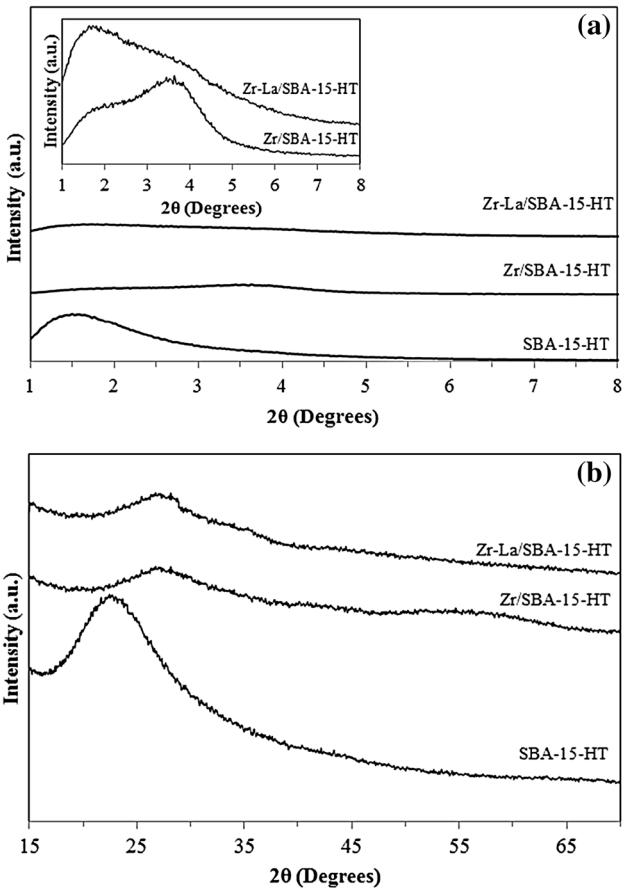

Fig. 2 XRD patterns of all samples obtained from the hydrothermal method at low-angle (**a**) and high-angle (**b**) regions

mesoporous silicas with two-dimensional hexagonal structure is confirmed by the presence of a basal (100) peak along with (110) and (200) reflections in the low-angle region after calcination of sample. Furthermore, we can note that, in the case after zirconium oxide loading, a shift of the XRD peaks toward high-angle region is evident indicating an increase in the unit cell parameter [26]. The expansion of unit cell parameter may indicate the successful incorporation of metal oxide in the framework. Similar results were previously observed [27]. However, in case of Zr-La/SBA-15-SG sample, the intensity of the diffraction peaks (100), (110) and (200) decreased or disappeared. This is probably due to the incorporation of bimetallic or heteroatoms into the framework of SBA-15 causes a slight collapse of the hexagonal structure [28]. With regard to the XRD patterns in the high-angle region (Fig. 1b), only wide diffraction peaks of characteristic of amorphous SiO_2 were observed with 2θ around 21-25° (broad) [29]. However, no any diffraction peak of metal oxide crystalline phases can be observed due to metal oxide has no aggregates on the surface of the samples. The samples prepared by hydrothermal method, as can be seen in Fig. 2, exhibit stronger peaks. The relative intensity of the (110) and (200) reflections disappear with compared to those prepared by sol–gel method. This may be due to extensive washing in the last step strongly reduces order of the pores. A possible explanation for this behavior could be that the template has a higher solubility in ethanol than in water, thus, ethanol leads to more efficient removal of the template as described by Ko and Bae [30, 31]. Besides, during extensive washing, the formation of blocked pores cannot be ruled out, which would offer a straight forward explanation for the significant reduction in surface area as well as the long range order in XRD [32]. This is in agreement with previous reports to claim that the well-ordered pore structure (100) was retained, but the intensity of the diffraction peaks (200) decreased probably due to destruction of the ordered structure [33, 34]. For Zr/SBA-15-HT and Zr-La/SBA-15-HT, the characteristic of diffraction peak is attenuated and slight change in the intensity with a pore system lacking long-range order when samples are incorporated with Zr and bimetallic Zr-La, pointing out the collapse of the mesostructure of the SBA-15, which is similar to those

of mesoporous SBA-15 silica synthesized with phosphoric acid [35] and cationic surfactant in presence of organic salts [36]. Figure 2b shows the high-angle XRD patterns of all samples. The XRD pattern of SBA-15 prepared by hydrothermal method was broad (amorphous SiO_2) because the sizes were very small. The result was similar as seen in Fig. 1b. Because there are no noticeable high-angle XRD patterns of these mesoporous silica materials, the pore walls are concluded to be amorphous in nature [37]. Thus, nitrogen sorption and XRD demonstrate that both sol–gel and hydrothermal methods have typical SBA-15 structures.

Figure 3 shows the nitrogen adsorption/desorption isotherms of SBA-15 samples prepared by sol–gel (a) and hydrothermal method (b). All samples exhibited type IV adsorption isotherms with a H1 hysteresis loop as defined by IUPAC classification, indicating that they are mesoporous materials. The isotherms for sol–gel method samples showed quite different pattern. Two inflection points and hysteresis loop moved toward lower pressure (P/P_0 = 0.3–0.7). Meanwhile, the isotherms for hydrothermal method samples, they presented hysteresis loop of type H1, occurring at higher relative pressure (P/P_0 = 0.7–0.9)

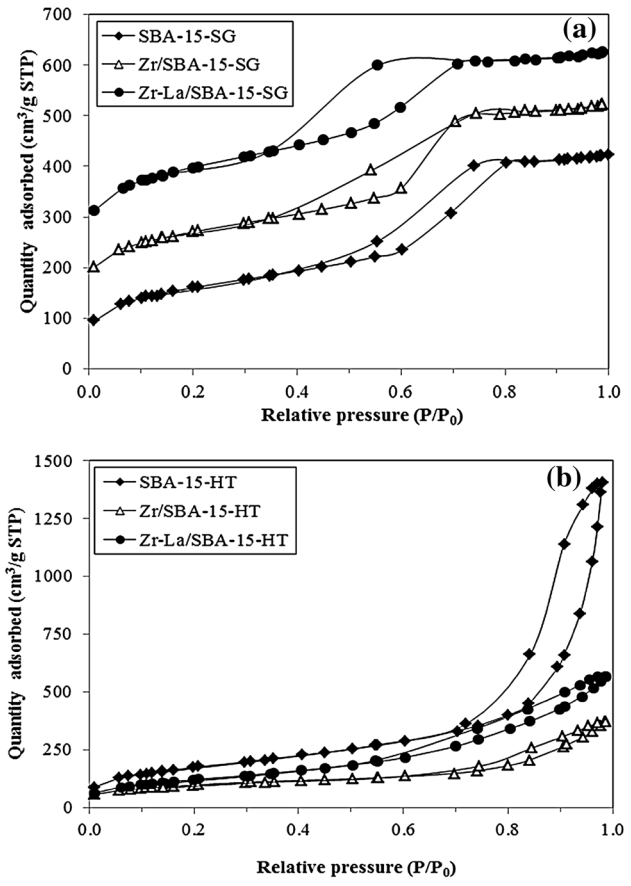

Fig. 3 Nitrogen adsorption/desorption isotherms of all samples synthesized by sol–gel (**a**) and hydrothermal methods (**b**)

corresponding to the capillary condensation of nitrogen. It indicates larger mesoporosity character of SBA-15, confirming that metal oxide can be located into the hexagonal framework of SBA-15 and the mesoporous channels still remain. The textural properties of the samples are summarized in Table 1 which the pore volume of SBA-15-SG, Zr/SBA-15-SG, and Zr-La/SBA-15-SG was 0.69, 0.70, and 0.72 cm^3/g, respectively. The incorporation of Zr and bimetallic Zr-La into SBA-15 increases the surface area due to the Zr and La were located on the external surfaces suggesting that metal oxide were not incorporated into the channels of SBA-15 or found on the external surfaces, leading to an increase in surface area. Moreover, even when some of the pores are blocked, it suggests that the Zr and La prepared by sol-gel method were still well dispersed in the SBA-15. The result was confirmed by the high-angle diffraction peak of XRD as shown in Fig. 1b. The effect has also been observed for mesoporous Al-SSP doped with Mo [38]. For SBA-15 samples prepared by hydrothermal method, the pore volume of samples was higher than the sol–gel method. The incorporation of Zr and bimetallic Zr-La into SBA-15 decreases the surface area, mainly due to the blockage of the mesoporous framework. This is probably due to for samples synthesized by hydrothermal method, agglomeration of primary particles altered the porous shape [39], resulting in metal oxide easily incorporated into the channels of SBA-15.

The pore size distribution (PSD) calculated by BJH method is shown in Fig. 4. In all samples prepared by sol–gel method, they have a narrow pore size distribution with an average pore diameter around 3.4–4.5 nm, confirming that the pore size distribution is in the mesoporous range. For the samples prepared by hydrothermal method, the distribution was broad and diameter was large. The pore diameter decreased from 11.2 to 5.3 nm as the incorporation of Zr and bimetallic Zr-La into SBA-15. It can be seen that the calculated pore size distribution was in good agreement with N_2 adsorption/desorption isotherms as mentioned above.

Table 1 Textural properties of the samples

Samples	Surface area (m2/g)	Average pore diameter (nm)	Average pore volume (cm^3/g)
SBA-15-SG	574	4.5	0.69
Zr/SBA-15-SG	611	4.1	0.70
Zr-La/SBA-15-SG	713	3.4	0.72
SBA-15-HT	638	11.2	2.20
Zr/SBA-15-HT	492	6.0	0.90
Zr-La/SBA-15-HT	445	5.3	0.89

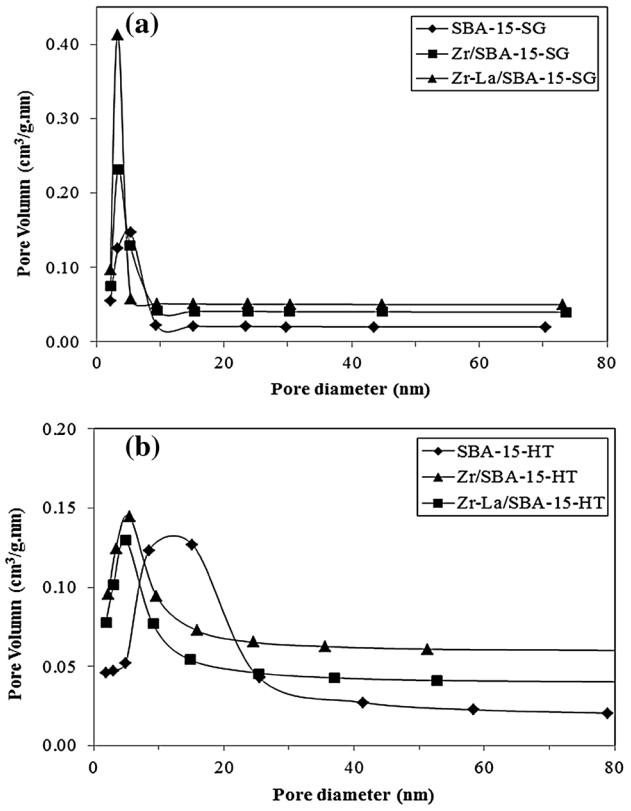

Fig. 4 BJH pore size distribution of all samples by sol–gel (**a**) and hydrothermal methods (**b**)

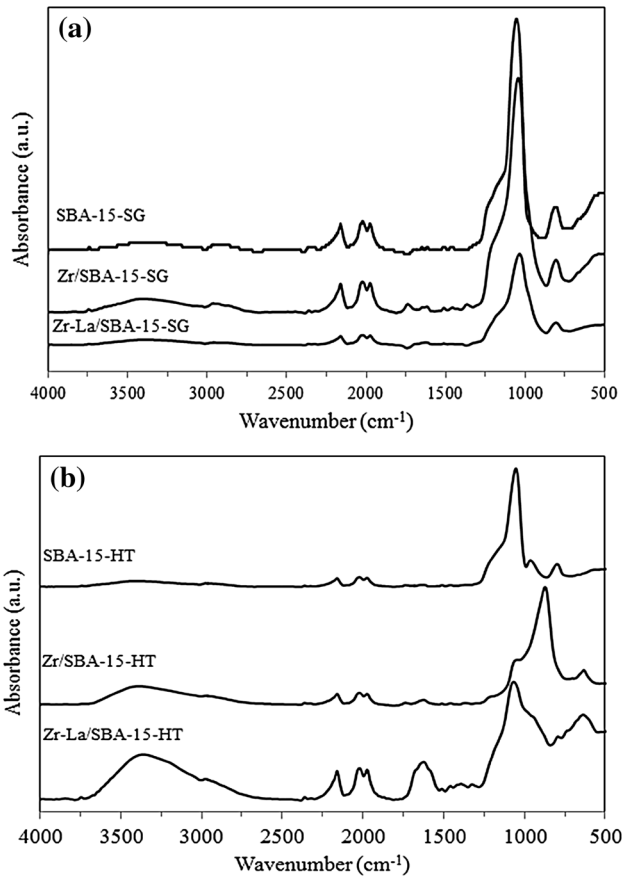

Fig. 5 FTIR spectra of all samples by sol–gel (**a**) and hydrothermal methods (**b**)

In order to further confirm the incorporation of zirconium and bimetallic zirconium-lanthanum ion into the framework, the samples prepared by sol–gel and hydrothermal methods were characterized with FTIR technique. The fundamental vibrations of the Zr–O–Si, Zr–La–O–Si and Si–O–Si bonds in the framework can be seen below 1300 cm^{-1}. The bands at 808 and 1054 cm^{-1} are assigned to the bending (or symmetric stretching), and asymmetric stretching of the intertetrahedral oxygen atoms in SiO_2 of SBA-15, respectively [14]. As shown in Fig. 5, the SBA-15 samples show absorption band at 3398–3412 cm^{-1} assigned to the stretching vibration of OH groups for physisorbed water molecules on SBA-15 surface [40]. The OH bond vibrations due to the presence of the silanol group also show a peak at the same wavenumber. An OH deformation vibration was observed near 1630 cm^{-1} [13]. The absence of C–H vibrations at 2850–3000 cm^{-1} indicates the efficient removal of the surfactant [41]. The FTIR studies of SBA-15 samples synthesized by sol–gel and hydrothermal methods confirm that there was no change in functional group after the incorporation of Zr and bimetallic Zr-La into SBA-15. For Zr/SBA-15-HT sample, this band shifts toward the lower wave number at 872 cm^{-1}. The shift of this absorption band toward the lower wavenumber is considered as an indication of metal incorporating into the framework of silica tetrahedral [42, 43]. Therefore, it indicates that the small particle size of Zr by hydrothermal may be partly incorporated into the framework of SBA-15 excepting for the Zr-La/SBA-15-HT. The intensity of the bands around 1624 cm^{-1} could be assigned to CH stretching vibration and asymmetric stretching vibration of the $NCOO^-$ skeletal vibration with La addition, indicating that bimetallic Zr and La have been successfully grafted onto the wall of SBA-15 [44, 45] corresponding to the low and high angle XRD results.

The Raman spectra of SBA-15 resemble those of published visible Raman spectra. As shown in Fig. 6a, the D_1 and D_2 bands at 248 and 386 cm^{-1} are assigned to symmetric O–Si–O motions of vibrationally isolated four-membered rings of SiO_4 tetrahedral and to breathing motions of three-membered rings of SiO_4 tetrahedral, respectively [46]. The combined feature at around 800 and 830 cm^{-1} is assigned to the transverse (TO) and longitudinal (LO) optical components of siloxane bridges network motions, respectively. In addition, the band at 976 cm^{-1} is assigned to the Si–OH stretching of free surface silanols [47]. For

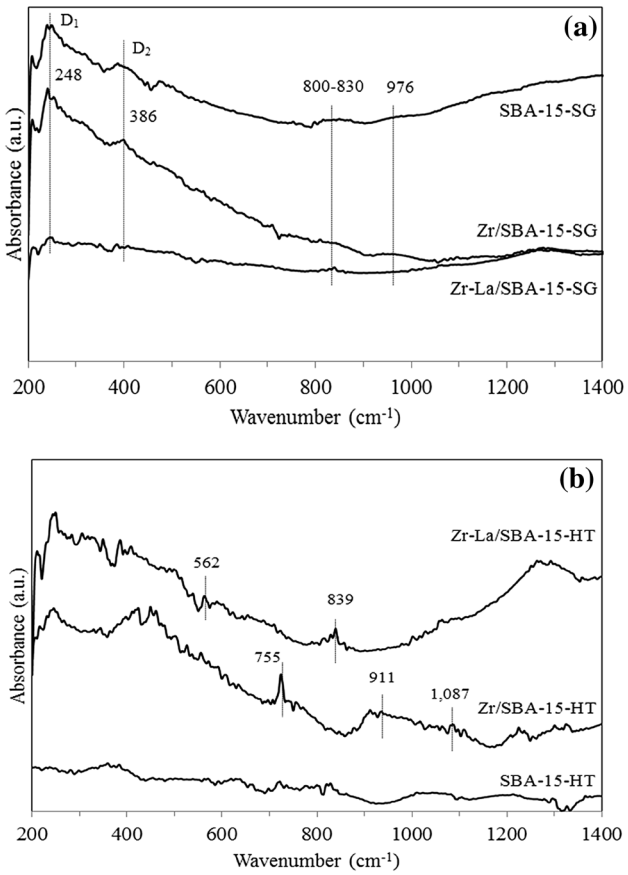

Fig. 6 Raman spectra of all samples by sol–gel (**a**) and hydrothermal methods (**b**)

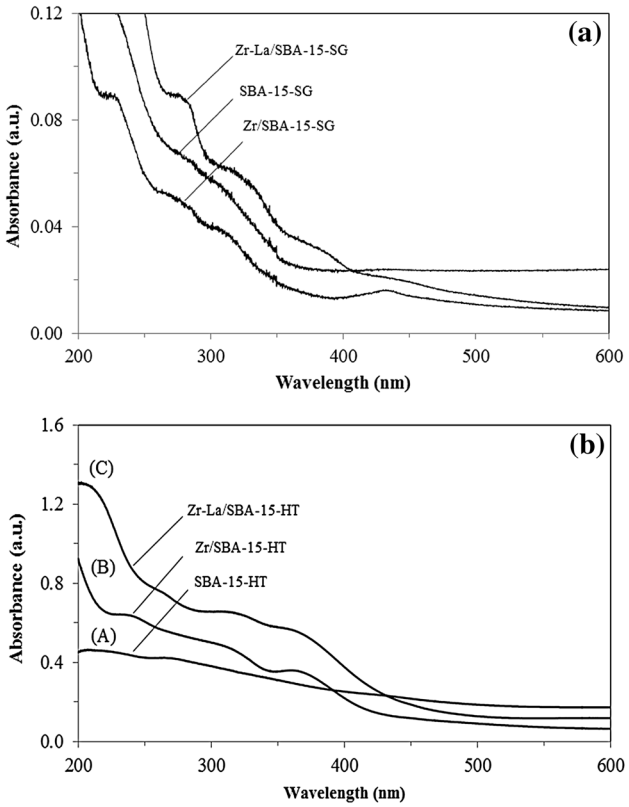

Fig. 7 UV–Vis diffuse reflectance spectra of all samples by sol–gel (**a**) and hydrothermal methods (**b**)

zirconium incorporated on SBA-15, no new peaks were observed indicating the monolayer coverage with no crystalline phase of zirconia species on the SBA-15. However, for Zr-La/SBA-15-SG sample, the intensity of the peaks corresponding to SBA-15 decreases dramatically due to the metal oxide found on the external surfaces, as supported by the textural properties results in Table 1. For samples prepared by hydrothermal method (Fig. 6b), the main Raman bands of tri-cyclosiloxane rings, siloxane bridges, and surface silanol groups were still remained, indicating that the metal oxide incorporated into the channels of SBA-15. For SBA-15-HT showing a weak band, this is identified as the D1 band of cyclic tetrasiloxane rings. Similar SBA-15 peaks were reported by Chamack et al. [27]. The Raman band at 911 cm^{-1} for the Zr/SBA-15-HT sample is assigned to the Si–O–Zr linkages, indicating that some Zr species interact with Si–OH to form Si–O–Zr bond [48]. According to the report [49], the bands at 755 and 1087 cm^{-1} may correspond to the intermediate phase of zirconia, and no Raman bands of tetragonal zirconia, monoclinic zirconia and zircon were observed. The results demonstrate that some Zr species on SBA-15 are amorphous zirconia, and are probably present as highly dispersed surface species [50]. For the Raman spectrum of Zr-La/SBA-15-HT, the band at 839 cm^{-1} is attributed to the perturbed silica vibrations for $Si(–O^–)_x$ functionalities, suggesting the formation of La–O–Si bond. The band at ~562 cm^{-1} is attributed to the lanthanum oxide overlaps with the Raman band of tri-cyclosiloxane rings [50]. Regarding the Raman characterization technique, it can be found that the metal oxide species can lead to partially M–OH species combine with Si–OH groups to form Si–O–M bond, which is in agreement with the results of FTIR spectroscopy.

Diffuse reflectance spectroscopy is a well-known method to detect the framework and extraframework of the transition metal ions. Figure 7 shows the UV–Vis absorption spectra of SBA-15 samples prepared by sol–gel (a) and hydrothermal method (b). No absorption band was observed on SBA-15 for both methods because SiO_2 is transparent in the test UV region [51, 52]. For Zr/SBA-15-SG, the absorption band was found to be around 230–248 nm. This is the characteristic of the ligand-to-metal charge transfer (LMCT) from O^{2-} to Zr^{4+} with an octahedral coordination state [53]. In the case of Zr-La/SBA-15-SG, a very sharp absorption band was detected at 250–260 nm for the mechanical mixture of SBA-15 and metal oxide, which is

assigned to the electronic transition from 5d orbit to 4f orbit of La^{3+} species. This is not affected by the coordination of La^{3+} in the Zr-La/SBA-15-SG framework [42]. The emergence of absorption band shifts toward at 270 nm higher than previous report [14], which is owing to the presence of La^{3+} species in the tetracoordinated of SBA-15 framework. In contrast to SBA-15 samples prepared by hydrothermal method, it displayed distinct absorbance in the UV range. The absorbance intensity increased with incorporation of Zr and bimetallic Zr-La into SBA-15. In addition, previous studies also suggested that substantial blue shift in absorbance was observed on the incorporation of Zr and bimetallic Zr-La samples as compared with pure metal oxide [28].

To examine the sample morphology, SEM technique was performed. The SEM micrographs of different samples are shown in Figs. 8 and 9. The structure of SBA-15 synthesized by sol–gel method is fiber-like or elongated silica fibers with the hexagonal prismatic morphology of the particles, formed by aggregates of fibers or rods connected into ropelike macrostructures. Similar SEM images were reported by Kosuge et al. [54]. The long fibers are obtained using stirring, while the rod like particles of SBA-15 can be obtained in the absence of stirring. After incorporated the SBA-15 with Zr and bimetallic Zr-La, it can be seen that there was no significant change in the morphology of samples. For those samples synthesized by hydrothermal method, the particles of SBA-15 show worm-like morphology and aggregate together, which is similar to an earlier report [37]. After incorporated with Zr and bimetallic Zr-La, it shows spherical particles together with some small irregular shape particles, indicating poor long-range ordered structures [55].

The dispersive X-ray spectroscopy (EDX) was also performed to determine the elemental distribution in the SBA-15 samples prepared by sol–gel and hydrothermal methods. All elements in the samples such as Si, O, Zr and La can be detected using the EDX mapping mode. The typical EDX mapping of Zr-La/SBA-15-SG and Zr-La/SBA-15-HT sample is shown in Fig. 10. In this figure, the distribution of Si, Zr and La was observed. The density of Si was strongly observed because Si is the main components of SBA-15 samples. After incorporated with Zr and bimetallic Zr-La, the well distribution of metal oxide was evident. For Zr-La/SBA-15-HT sample, agglomeration of metal oxide particles

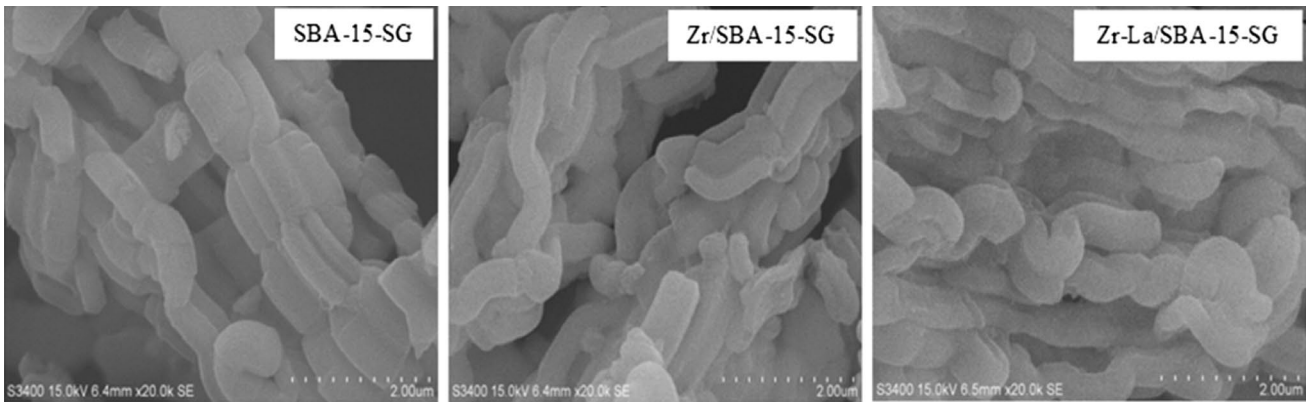

Fig. 8 SEM images of all samples obtained from the sol–gel method

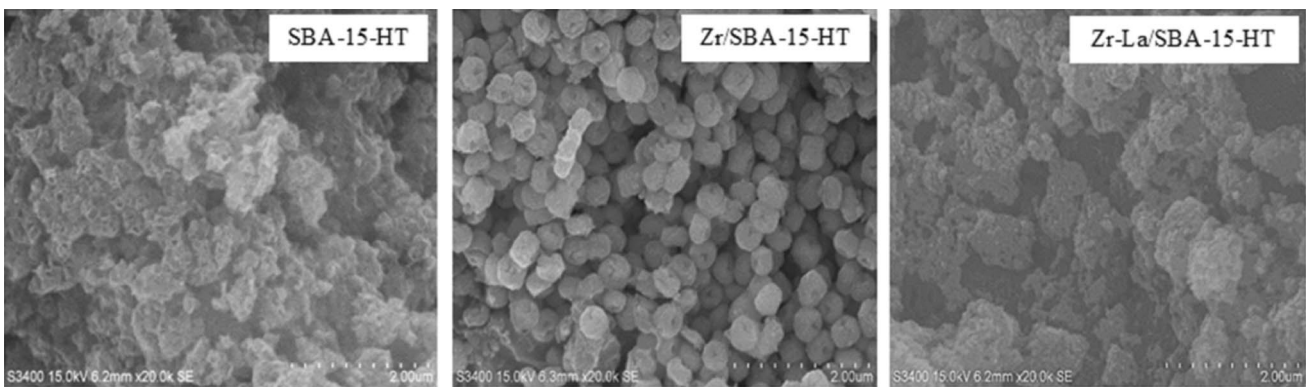

Fig. 9 SEM images of all samples obtained from the hydrothermal method

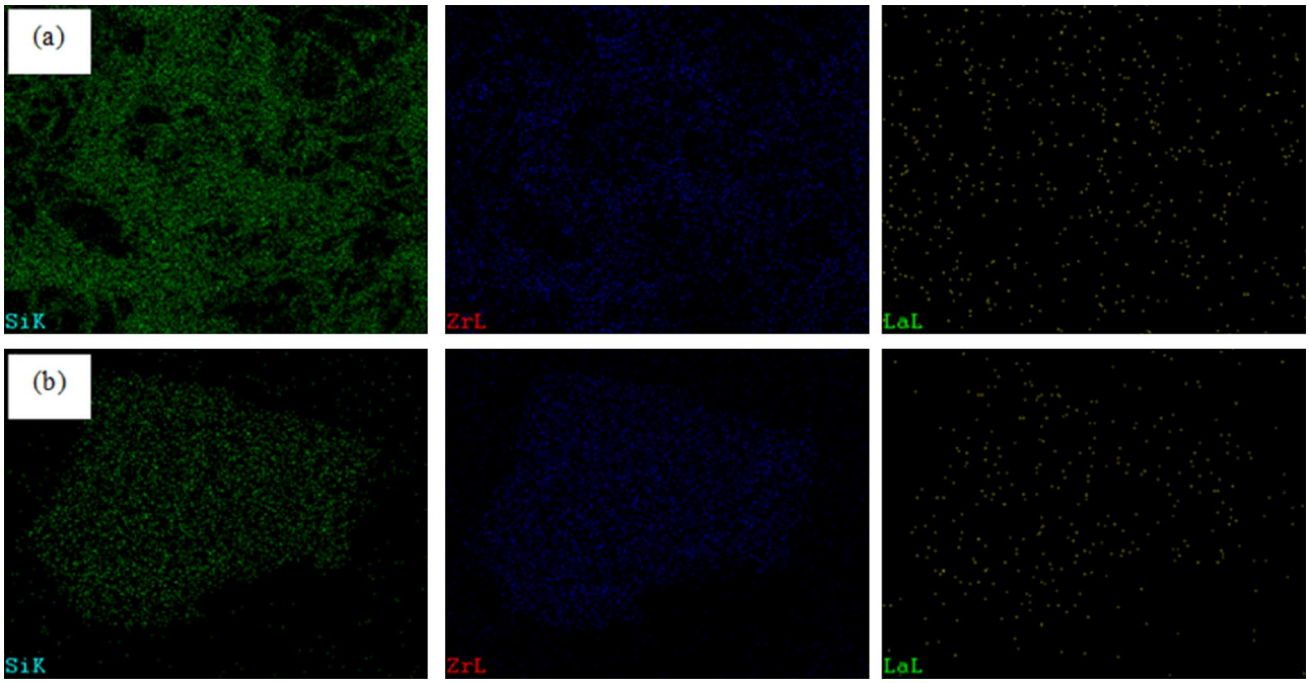

Fig. 10 The typical EDX mapping of Zr-La/SBA-15-SG (**a**) and Zr-La/SBA-15-HT (**b**) sample

Table 2 The amount of each element near the surface of catalyst granule obtained from EDX

Samples	Amount of weight on surface (wt%)			
	Si	O	Zr	La
SBA-15-SG	50.2	49.8	0	0
Zr/SBA-15-SG	37.4	43.4	19.2	0
Zr-La/SBA-15-SG	37.7	41.3	19.3	1.7
SBA-15-HT	48.1	51.9	0	0
Zr/SBA-15-HT	13.0	35.6	51.4	0
Zr-La/SBA-15-HT	12.8	35.3	46.4	5.5

was found mostly on outer surface. This result is in accordance with that obtained from XRD.

The amount of each element near the surface of catalyst granule can be determined quantitatively. The results are summarized in Table 2. The key elements to be considered are Zr and bimetallic Zr-La. For both synthesized SBA-15 samples, the percentage of silica decreased due to conceal with metal oxide particle. For those samples synthesized by hydrothermal method, the percentage variation of metal oxide (especially Zr element) is higher than the percentage variation of samples synthesized by sol–gel method. Therefore, this result can be ascribed to amount of metal oxide loading to exceeding monolayer content, which may block the pore on surface or attach into the pore [56]. Thus, for the detected value of samples synthesized by hydrothermal method, metal oxide was easily incorporated into the channels of SBA-15. Moreover, the EDX has limit detection about 5 microns from the surface, which cannot detect deep metal oxide in the pore.

The morphological features of the samples prepared by sol–gel and hydrothermal method were studied by TEM technique. As shown in Fig. 11, the synthesized SBA-15 by sol–gel clearly indicated that the samples retained the uniform hexagonal mesostructured pores shape. The arrangement of these mesopores is rather ordered, showing a long-range ordering of the mesostructure. In the TEM image of Zr-La/SBA-15-SG, in the boundary region of the crystal study, the mesostructure is highly ordered. However, in the center area, the arrangement of pore system is rather disordered. This is in agreement with previous reports that the sample with high zirconium content Si/Zr = 5 may result in diminishing of the structural regularity of the solid [14], which is in a good agreement with the result of the low-angle XRD result. For the synthesized SBA-15 by hydrothermal method (Fig. 12), the pore size of the samples was remarkably larger than that of the samples synthesized by sol–gel without well-ordered hexagonal mesopores, suggesting that the framework of hexagonal ordering was not preserved after the hydrothermal method. In addition, all samples cause broadening of the peaks and decrease the diffraction peak intensity (Fig. 2a), indicating the decrease of crystallinity, but not the collapse in the pore structure of the mesoporous [57]. It should be emphasized that the agglomeration of primary particles obtained from the hydrothermal method exhibited the porous shape, which

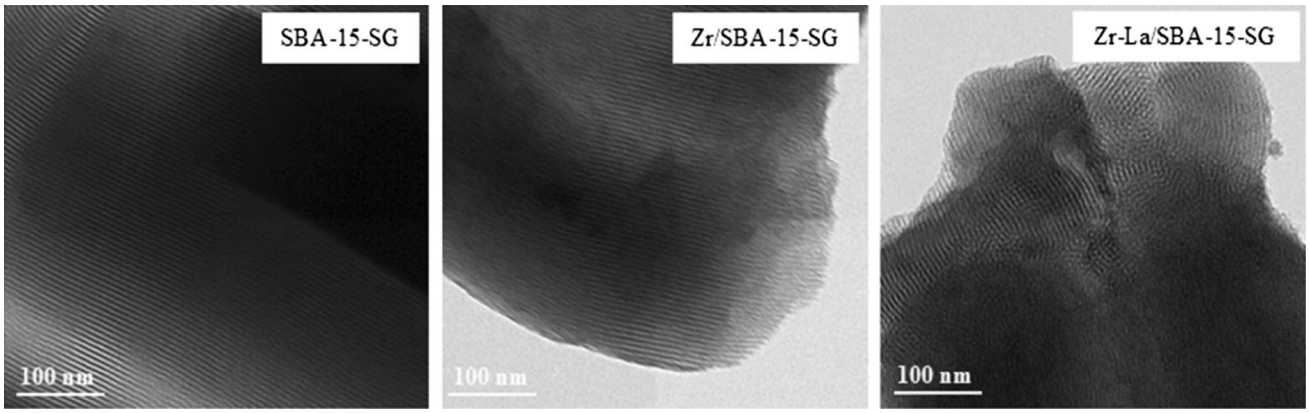

Fig. 11 TEM micrographs of all samples obtained from the sol–gel method

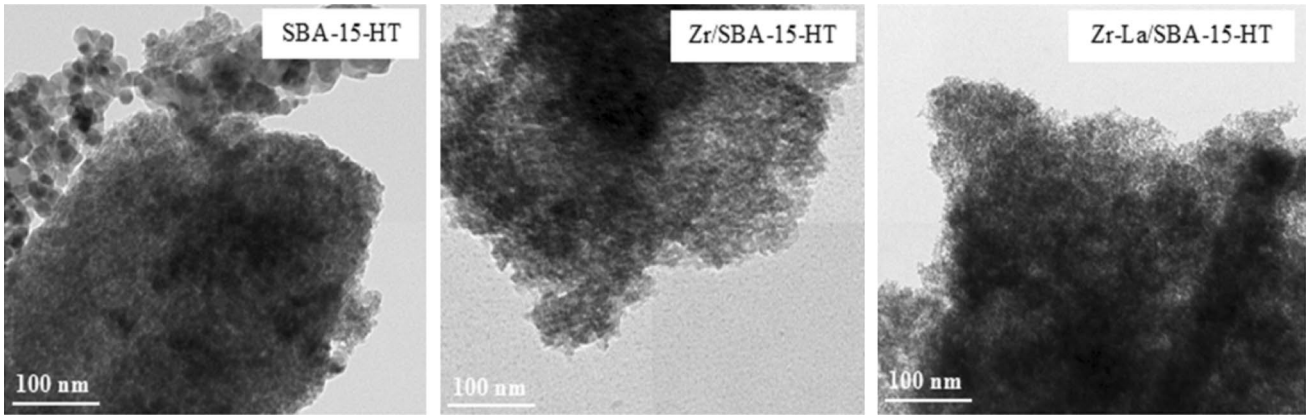

Fig. 12 TEM micrographs of all samples obtained from the hydrothermal method

is quite different from previous reports [15]. This phenomenon could be attributed to their distinguishable synthesis conditions. Conventional SBA-15 is prepared by sol–gel in strongly acidic media, while the samples prepared by hydrothermal method are synthesized in near neutral condition with high temperature and high pressure. The results were in agreement with those obtained by low-angle XRD and N_2 adsorption/desorption presented in Table 1.

The surface acidity of the samples was measured by NH_3 temperature-programmed desorption (NH_3-TPD) between 100 and 550 °C. Table 3 shows the number of acid site on samples calculated by integration of desorption areas of ammonia according to the Gauss curve fitting method, which are related to the acid sites on the samples. The TPD profiles (data not shown) for all samples indicated two different types of acid site. The assignment of desorption peaks between 175 and 300 °C is weak acid sites and the desorption peaks occurred above 300 °C refer to medium-strong acid sites [24]. Although NH_3-TPD technique has some drawbacks [4], it is fast, simple, and frequently employed method to evaluate the acidity. Firstly, the synthesized SBA-15-SG exhibits the lowest amount of weak acid site. The incorporation of Zr and bimetallic Zr-La into SBA-15 increases the weak and total acid sites. It can be observed that the Zr and bimetallic Zr-La can alter the acidity of SBA-15, demonstrating the suitable dispersion of the active phase. This can be attributed to the Zr^{4+} ions diameter (0.084 nm) and La^{3+} ions diameter

Table 3 The surface acidity of all samples from NH_3-TPD

Samples	Number of acid site (μmole NH_3/g cat.)		
	Weak acid sites	Medium-strong acid sites	Total acid site
SBA-15-SG	31.3	470.4	501.7
Zr/SBA-15-SG	251.4	314.3	565.7
Zr-La/SBA-15-SG	324.1	412.1	736.2
SBA-15-HT	177.8	928.7	1106.5
Zr/SBA-15-HT	830.9	942.1	1773.0
Zr-La/SBA-15-HT	451.8	662.2	1114.0

(0.272 nm) is much larger than that of Si^{4+} ion (0.026 nm) when smaller Si^{4+} ions are replaced by larger Zr^{4+} and La^{3+} ions in the framework of the solid. The bond length of Zr–O–Si and Zr–La–O–Si clearly differs from the one of Si–O–Si [14, 58], which is corresponding to the Brønsted acid sites. It should be noted that the amount of weak acid site is probably more related to the Brønsted acid site, whereas Lewis acid site is more related to the strong acid site [59]. For SBA-15 samples prepared by hydrothermal method, an increase in the acidity was found when the sample is incorporated with Zr. However, the incorporation of bimetallic Zr-La into SBA-15 did not improve the total acidity (decreased from 1773 to 1114 μmole NH_3/g cat.), which could be described by the reduction of its surface area, blocking of NH_3 molecules in which the amount of acid sites decreases. It appears that the alteration of acidity of these materials can be useful to further apply for catalytic reactions, where acid sites are necessary such as alcohol dehydration or esterification.

4 Conclusion

In the present work, zirconium (Zr) and bimetal (Zr and La) containing mesoporous silicas (SBA-15) were synthesized by conventional sol–gel and one-step hydrothermal methods without addition of hydrochloric acid. The influence of synthesis method on the structure and characteristics of these materials has been investigated. It appears that the samples obtained from the sol–gel method retain the two-dimensional hexagonal order structure of siliceous SBA-15 material. In contrast to samples obtained from the hydrothermal method, the characteristic diffraction peak was slightly changed in the intensity with a pore system lacking long-range order. The incorporation of Zr and bimetal (Zr and La) had an effect on the textural properties for both methods. For those samples synthesized by sol–gel method, they consisted of agglomerated particles with primarily irregular shape with the metal oxide located on the external surfaces. For samples synthesized by hydrothermal method, the agglomeration of primary particles altered the porous shape. Besides, this hydrothermal method still had some outstanding advantages, such as environmental friendly with avoiding of toxic reagents and making new active sites, especially Brønsted acid types. Thus, SBA-15 synthesized by both methods provided a better and more practical than the existing methodologies with their potential and better applications when acid sites are required.

Acknowledgements The authors thank the Grant for International Research Integration: Chula Research Scholar, Ratchadaphiseksomphot Endowment Fund for financial support of this project.

References

1. Y. Wan, D.Y. Zhao, Chem. Rev. **107**, 2821 (2007)
2. Y. Han, D. Zhang, Curr. Opin. Chem. Eng. **1**, 129 (2012)
3. H.C. Xin, J. Zhao, S.T. Xu, J.P. Li, W.P. Zhang, X.W. Guo, E.J.M. Hensen, Q.H. Yang, C. Li, J. Phys. Chem. C **114**, 6553 (2010)
4. H.C. Xin, X.P. Li, Y. Fang, X.F. Yi, W.H. Hu, Y.Y. Chu, F. Zhang, A.M. Zheng, H.P. Zhang, X.B. Li, J. Catal. **312**, 204 (2014)
5. Q.H. Yang, J. Liu, L. Zhang, C. Li, J. Mater. Chem. **19**, 1945 (2009)
6. C. Li, H.D. Zhang, D.M. Jiang, Q.H. Yang, Chem. Commun. **43**, 547 (2007)
7. Q.H. Yang, D.F. Han, H.Q. Yang, C. Li, Chem. Asian J. **3**, 1214 (2008)
8. H.C. Xin, X.P. Li, L. Chen, Y. Huang, G.R. Zhu, X.B. Li, Energy. Environ. Focus **2**, 18 (2013)
9. C.T. Kresge, M.E. Leonowicz, W.J. Roth, J.C. Vartuli, S.J. Beck, Nature **359**, 710 (1992)
10. N. Rahmat, A.Z. Abdullah, A.R. Mohamed, Am. J. Appl. Sci. **7**, 1579 (2010)
11. H.C. Xin, Q.H. Yang, Petrochem. Technol. **35**, 1017 (2006)
12. G. Lapisardi, F. Chiker, F. Launay, J.P. Nogier, J.L. Bonardet, Micropor. Mesopor. Mater. **78**, 289 (2005)
13. H.C. Xin, Y. Fang, X. Li, Energy Environ. Focus **3**, 287 (2014)
14. P. Salas, J.A. Wang, H. Armendariz, C. Angeles-Chavez, L.F. Chen, Mater. Chem. Phys. **114**, 139 (2009)
15. X. Sheng, Y. Zhou, Y. Duan, Y. Zhang, M. Xue, J. Porous. Mater. **18**, 677 (2011)
16. J. Liu, Y. Liu, W. Yang, H. Guo, H. Zhang, Z. Tang, F. Fang, Mater. Lett. **128**, 15 (2014)
17. E. Brzozowski, M.S. Castro, J. Eur. Ceram. Soc. **20**, 2347 (2000)
18. E.K. Nyutu, C.H. Chen, P.K. Dutta, S.L. Suib, J. Phys. Chem. C **112**, 9659 (2008)
19. O. Mekasuwandumrong, N. Wongwaranon, J. Panpranot, P. Praserthdam, Mater. Chem. Phys. **111**, 431 (2008)
20. Y. Deng, X. Zhou, G. Wei, J. Liu, C.W. Nan, S. Zhao. J. Phys. Chem. Solids **63**, 2119 (2002)
21. Y. Deng, G.D. Wei, C.W. Nan, Chem. Phys. Lett. **368**, 639 (2003)
22. A. Orlov, Q.Z. Zhai, J. Klinowski, J. Mater. Sci. **41**, 2187 (2006)
23. D.Y. Zhao, J. Sun, Q. Li, G.D. Stucky, Chem. Mater. **12**, 275 (2000)
24. J.A. Cecilia, C.G. Sancho, J.M.M. Robles, J.S. Gonzalez, R.M. Tost, P.M. Torres, Catal. Today. **254**, 43 (2015)
25. E.P. Barrett, L.G. Joyner, P.P. Halenda, J. Am. Chem. Soc. **73**, 373 (1951)
26. X. Sheng, Y. Zhou, Y. Duan, J. Porous. Mater. **18**, 677 (2011)
27. M. Chamacka, A.R. Mahjouba, H. Aghayanba, Chem. Eng. Res. Des. **94**, 565 (2015)
28. Y. Tang, E. Zong, H. Wan, Z. Xu, S. Zheng, D. Zhu, Microporous Mesoporous Mater. **155**, 192 (2012)
29. S. Chytil, W.R. Glomm, E.A. Blekkan, Catal. Today **147**, 217 (2009)
30. M. Kruk, M. Jaroniec, C.H. Ko, R. Ryoo, Chem. Mater. **12**, 1961 (2000)
31. Y.K. Bae, O.H. Han, Microporous Mesoporous Mater. **106**, 304 (2007)
32. J.P. Thielemann, F. Girgsdies, R. Schlog, C. Hess, Beilstein J. Nanotechnol. **2**, 110 (2011)
33. G. Chandrasekar, K.S. You, J.W. Ahn, W.S. Ahn, Microporous Mesoporous Mater. **111**, 455 (2008)
34. M. Halina, S. Ramesh, M.A. Yarmo, R.A. Kamarudin, Mater. Chem. Phys. **101**, 344 (2007)

35. B. Wu, Z. Tong, X. Yuan, J. Porous Mater. **19**, 641 (2012)
36. R. Ryoo, J.M. Kim, C.H. Ko, C.H. Shin, J. Phys. Chem. **100**, 17718 (1996)
37. X. Pang, F. Tang, Microporous Mesoporous Mater. **85**, 1 (2005)
38. T. Chanchuey, C. Autthanit, B. Jongsomjit, J. Chem. 2016 (2016)
39. M. Wannaborworn, P. Praserthdam, B. Jongsomjit, J. Nanomater. **16**, 429 (2015)
40. S. Bendou, M. Amrani, J. Miner. Mater. Char. Eng. **2**, 404(2014)
41. N.S. Sanjini, S. Velmathi, RSC Adv. **4**, 15381 (2014)
42. K.S.W. Sing, D.H. Everett, R.A.W. Haul, L. Moscow, R.A. Pierotti, J. Rouquerol, T. Siemieniewska, Pure. Appl. Chem. **57**, 603 (1985)
43. S.C. Laha, P. Mukherjee, S.R. Sainkar, R. Kumar, J. Catal. **207**, 213 (2002)
44. L. Qian, Z. Ma, Y. Ren, H. Shi, B. Yue, S. Feng, J. Shen, S. Xie, Fuel **122**, 47 (2014)
45. R. Kishor, A.K. Ghoshal, RSC Adv. **6**, 898 (2016)
46. A. Rahmani, M. Benoit, C. Benoit, Phys. Rev. B Condens. Matter Mater. Phys. **68**, 184202 (2003)
47. B.A. Morrow, A.J. McFarlan, J. Non-Cryst. Solids **120**, 61 (1990)
48. X. Gao, J.L.G. Fierro, I.E. Wachs, Langmuir **15**, 3169 (1999)
49. M. Zhang, E.K. Salje, G.C. Capitani, H. Leroux, A.M. Clark, J. Schluter, R.C. Ewing, J. Phys, Condens. Matter. **12**, 3131 (2000)
50. H. Li, J. Ren, X. Qin, Z. Qin, J. Lin, Z. Li, RSC Adv. **5**, 96504 (2015)
51. T. Klimova, O. Gutierrez, L. Lizama, J. Amezcua, Microporous Mesoporous Mater. **133**, 91(2010)
52. S. Wu, Y. Han, Y.C. Zou, J.W. Song, L. Zhao, Y. Di, S.Z. Liu, F.S. Xiao, Chem. Mater. **16**, 486 (2004)
53. S.Y. Chen, H.D. Tsai, W.T. Chuang, J.J. Lee, C.Y. Tang, C.Y. Lin, S. Cheng, J. Phys. Chem. C **113**, 15226 (2009)
54. K. Kosuge, T. Sato, N. Kikukawa, M. Takemori, Chem. Mater. **16**, 899 (2004)
55. J. Wang, L. Fang, F. Cheng, X. Duan, R. Chen, J. Nanomater **112**, 128–133 (2013)
56. F. El Kady, S. Shaban, A.A. El Naga, Transit. Metal. Chem. **36**, 237 (2011)
57. Y. Li, B. Yan, H. Yang, J. Phys. Chem. C **112**, 3959 (2008)
58. Advances in Dielectric Materials and Electronic Devices, ed. By K.M. Nair, R. Guo, A.S. Bhalla, D. Suvorov, S.I. Hirano (Wiley, Maryland, USA, 2005), p. 208
59. J. Handzlik, J. Ogonowski, J. Stoch, M. Mikotajczyk, P. Michorczyk, Appl. Catal. A **312**, 213 (2006)